Journal Name

ARTICLE

A Low-cost Cementite (Fe_3C) Nanocrystals@N-doped Graphitic Carbon Electrocatalyst for Efficient Oxygen Reduction

Received 00th January 20xx,
Accepted 00th January 20xx

DOI: 10.1039/x0xx00000x

www.rsc.org/

Tianxing Wu,[a] Haimin Zhang,*[a] Xian Zhang,[a] Yunxia Zhang,[a] Huijun Zhao[a,b] and Guozhong Wang*[a]

In this work, chitosan whiskers (CWs) were first extracted using low-cost and earth-abundant crab shells as material by a series of chemical processes, then assembled into chitosan whisker microspheres (CWMs) *via* a simple photochemical polymerization approach. Subsequently, cementite (Fe_3C) nanocrystal@N-doped graphitic carbon (Fe_3C@NGC) nanocomposite was successfully fabricated by high temperature pyrolysis of CWMs adsorbed with ferric acetylacetonate ($Fe(acac)_3$) at 900 °C. It was found that a suitable growth atmosphere generated inside CWMs during high temperature pyrolysis is critically important to form Fe_3C nanocrystal cores, concurrently accompanying a structure transformation from chitosan whiskers to mesoporous graphitic carbon shells with natural nitrogen (N) doping property, resulting in the formation of core-shell structure Fe_3C@NGC nanocomposite. The resulting samples were evaluated as electrocatalysts for oxygen reduction reaction (ORR). In comparison with sole N-doped graphitic carbon without Fe_3C nanocrystals obtained by direct pyrolysis of chitosan whisker microspheres at 900 °C (CWMs-900), Fe_3C@NGC showed significantly improved ORR catalytic activity. The tolerance to fuel cell molecule (*e.g.*, methanol) and durability of Fe_3C@NGC is obviously superior to commercial Pt/C catalyst in alkaline media. The high ORR performance of Fe_3C@NGC could be due to its large surface area (313.7 $m^2\ g^{-1}$) and a synergistic role of Fe_3C nanocrystals and N doping in graphitic carbon creating more catalytic active sites, and a porous structure of nanocomposite facilitating mass transfer to efficiently improve the utilization of these catalytic active sites.

Introduction

Design and development of low-cost and abundant non-precious metal catalysts with oxygen reduction reaction (ORR) activity are critically important to replace expensive and scarce Pt-based catalysts for practical application of future fuel cell devices. Among all reported to date non-precious metal ORR catalysts, carbon-based materials including heteroatom-doped/co-doped carbon structures, carbon-based composites with metal chalcogenides, nitrides, carbides and phosphides, have been promising candidates to replace Pt-based catalysts for ORR application.[1]

Currently, the most concerned issues of researchers on ORR catalysts are mainly concentrated on two aspects, namely, creating more catalytic active sites and fully utilizing these catalytic active sites. The amount of catalytic active sites of a catalyst is closely related to material chemical composition and interactions between different components, while the utilization efficiency of catalytic active sites is highly dependent on material structure property (*e.g.*, pore structure).[2] Therefore, it is considerably crucial to design and develop ORR catalysts with effective chemical composition creating more catalytic active sites and suitable pore structures enabling full utilization of the generated catalytic active sites.

It is well known that cementite (Fe_3C) is a superior magnetic material owing to its ferromagnetism and magnetic transformation characteristics.[3] Recently, some studies have demonstrated that Fe_3C-based materials possess many potential applications in different areas, such as lithium batteries, generation of bioelectricity, microwave absorbents, detection of hydrogen peroxide, and fuel cells.[4,5] It is worth noting that the introduction of carbon nanostructures (*e.g.*, nanotubes, nanofibers, 3D carbon skeleton) in these Fe_3C-based materials plays an important role in improving their application performance.[2,5,6] Particular attention has been paid recently to develop Fe_3C nanoparticles embedded carbon nanostructure (*e.g.*, nanotubes, nanofibers) composites as electrocatalysts for ORR, exhibiting superior ORR catalytic activity.[2,6-8] Guo *et al.* reported the synthesis of bamboo-like carbon nanotube/Fe_3C nanoparticle hybrids by simply annealing a mixture of PEG-PPG-PEG Pluronic P123, melamine, and $Fe(NO_3)_3$ at 800 °C in N_2, as electrocatalysts, exhibiting high ORR catalytic activity and catalytic stability in alkaline and acidic medias.[7] Also, Yu and co-workers recently developed Fe_3C nanoparticles embedded mesoporous Fe-N-doped carbon nanofibers by pyrolyzation approach for ORR application, indicating comparable ORR catalytic performance to commercial Pt/C catalyst in alkaline media and good ORR performance in acidic media.[2] The superior ORR performance in both acidic and alkaline media can be due to a

[a] *Key Laboratory of Materials Physics, Centre for Environmental and Energy Nanomaterials, Anhui Key Laboratory of Nanomaterials and Nanostructures, Institute of Solid State Physics, Chinese Academy of Sciences, Hefei 230031, P. R. China. E-mail: zhanghm@issp.ac.cn, gzhwang@issp.ac.cn.*
[b] *Centre for Clean Environment and Energy, Gold Coast Campus, Griffith University, Queensland 4222, Australia.*

† Electronic Supplementary Information (ESI) available: BET data，FT-IR spectra，additional SEM image and XRD characterisation are included. See DOI: 10.1039/x0xx00000x

synergistic role of Fe_3C nanocrystals and N doping in carbon nanofiber structure creating more catalytic active sites. Additionally, the mesoporous structures of nanocomposite not only contribute high surface area, also improve mass transfer properties of ORR-related species in electrolytes, enabling full utilization of the generated catalytic active sites.[2,9] The aforementioned Fe_3C-based ORR catalysts have revealed that the introduction of carbon nanostructures can effectively improve electrical conductivity and additionally contribute catalytic active sites owing to heteroatom doping (*e.g.*, N), thus significantly enhancing ORR performance.[2,6] Although the reported Fe_3C@carbon composites to date have demonstrated great potential for ORR application, almost all studies are exclusively using chemicals as precursors to synthesize carbon nanostructure frames, undoubtedly increasing their practical application cost for future fuel cell devices.[2,6,7] Therefore, it is great importance of directly utilizing low-cost and earth-abundant biomass as material to fabricate natural heteroatom (*e.g.*, N) doped carbon nanostructure with Fe_3C nanocrystal encapsulation as high-performance ORR electrocatalyst.

Herein, chitosan whiskers (CWs) were first extracted from crab shells by a series of chemical processes (Scheme 1). Subsequently, chitosan whisker microspheres (CWMs) were assembled by dispersed chitosan whiskers using a photochemical polymerization approach with poly-vinylpyrrolidone (PVP) and 2,2-azo-bisisobutyronitrile (AIBN) as polymerization reagents (Scheme 1). Further, the formed CWMs after adequately adsorbing ferric acetylacetonate ($Fe(acac)_3$) were thermally treated at 900 °C in N_2, resulting in the formation of core-shell structure Fe_3C nanocrystal@N-doped graphitic carbon (Fe_3C@NGC) nanocomposite after HCl treatment (Scheme 1). Importantly, it was found that the chitosan whisker microspheres during high temperature pyrolysis can build an internal suitable growth atmosphere inside microspheres, favorable for the formation of Fe_3C nanocrystal cores of nanocomposite, and concurrently accompanying a structure transformation from chitosan whiskers to mesoporous graphitic carbon structure shells with natural nitrogen (N) doping property. However, the microsphere surface adsorbed $Fe(acac)_3$ was found to be prone to form independent iron oxides (Fe_mO_n) particles during high temperature pyrolysis possibly due to the presence of surface rich O-containing function groups. The resulting Fe_3C@NGC as electrocatalyst shows superior ORR catalytic activity in alkaline media. For comparison, sole N-doped graphitic carbon nanoparticles without Fe_3C nanocrystals (CWMs-900) were also prepared through high temperature pyrolyzing chitosan whisker microspheres for ORR measurements.

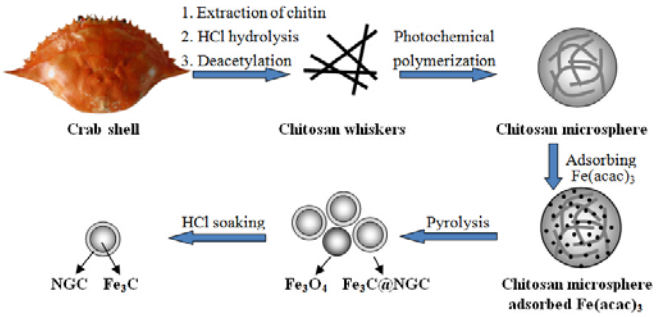

Scheme 1. Synthetic processes of Fe_3C@NGC nanocomposite.

Experimental

Chemicals.

Azodiisobutyronitrile (AIBN), polyvinylpyrrolidone (PVP), divinylbenzene (DVB) and ferric acetylacetonate ($Fe(acac)_3$) were purchased from Aladdin Reagent Company, acetic acid (CH_3COOH), hydrochloric acid (HCl), sodium hypochlorite ($NaClO_2$), sodium borohydride ($NaBH_4$), anhydrous ethanol (C_2H_5OH) and potassium hydroxide (KOH) were purchased from Sinopharm Chemical Reagent Co., Ltd. Commercial E-TEK Pt/C catalyst was purchased from Alfa Aesar. All the chemicals were used as received without further purification.

Extracting chitin from crab shells.

Crab shells after being washed and dried were smashed into small particles by a ball mill, then sieved (100 mesh), followed by deproteinization, taking off the inorganic salt and decoloration. 25 g of smashed crab shell was put into a 250 mL of round bottom flask, subsequently added 150 mL of 5% KOH solution, refluxed for 6 h at 100 ^{o}C in oil bath, then centrifuged after reaction and washed with adequate deionized water until pH value of the filtrate was close to neutral. The obtained solid was transferred into the round bottom flask, subsequently added 200 mL of 1.0 mol L^{-1} HCl, refluxed for 0.5 h at 100 ^{o}C in oil bath, then centrifuged after reaction and finally washed with deionized water until pH value of the filtrate was close to neutral. Next, 150 mL of 0.3% $NaClO_2$ solution was added into a round bottom flask, slowly added 5.0 mL of 0.1 mol L^{-1} HAc into the above solution to adjust the solution pH to 4-5, then the collected solid product from last step was dispersed into the above mixed solution, then stirred evenly, refluxed for 3 h at 70 ^{o}C in oil bath, finally centrifuged after reaction and washed with deionized water until pH value of the filtrate was close to neutral. Finally, pure chitin was collected by freeze-drying technique and preserved for further use.

Transforming chitin into chitosan whiskers.

4.0 g of pure chitin was first put into a 250 mL of round bottom flask, then added 120 mL of 3.0 mol L^{-1} HCl, refluxed for 3 h at 105 ^{o}C in oil bath, finally centrifuged after reaction and washed with adequate deionized water until pH value of the filtrate was close to neutral. The obtained solid product was then transferred into another round bottom flask, added a mixed solution including 50 mL of 50 w/v% NaOH and 10 mL of 0.5 w/w% $NaBH_4$, refluxed for 4 h at 120 ^{o}C in oil bath, finally centrifuged after reaction and washed with adequate deionized water until pH value of the filtrate was close to neutral. Chitosan whiskers were collected by freeze-drying technique and preserved for further use.

Chitosan whiskers assembling into chitosan whisker microspheres.

0.5 g of PVP and 0.2 g of AIBN were first dissolved into 60 mL of anhydrous ethanol. Then, 0.1 g of chitosan whisker sample and 2.0 mL of DVB were respectively added into the above solution under magnetic agitation. Subsequently, the above mixture was irradiated using two 8-W 365-nm UV lamps (from Philips) with a UV light intensity of 0.83 mW cm^{-2} for 24 h under continuously stirring at room temperature. During reaction, the clear solution gradually

became turbid, and finally a milk white emulsion was obtained. The resulting product was collected by centrifugation, and then adequately washed with deionized water and anhydrous ethanol, respectively. Finally, the sample was dried in a drying oven at 50 °C for 12 h and collected for further use.

Preparation of Fe_3C nanocrystal@N-doped graphitic carbon (Fe_3C@NGC).

1.0 g of $Fe(acac)_3$ was fully dissolved into 30 mL of anhydrous ethanol, 0.2 g of chitosan microspheres was added into the above solution, continuously agitation for 12 h to make the chitosan microspheres adsorb $Fe(acac)_3$ fully. After that, the samples were collected by centrifugation, washed with anhydrous ethanol three times, then dried in a drying oven at 50 °C for future use. Certain amount of samples was added into a rail boat and placed in a tube furnace. This was followed by flushing the furnace with high purity nitrogen (99.99%) for 30 minutes before heating to 900 °C at a heating rate of 5 °C min^{-1}, and kept at 900 °C for 4 h. After that the furnace was cooled down to room temperature, the resultant black products were added into 2 mol L^{-1} HCl and oscillated for 12 h, then centrifuged, washed with deionized water three times, dried in a drying oven at 50 °C for future use.

Characterizations.

The morphology and structure of samples were characterized by field emission scanning electron microscopy (FESEM, Quanta 200FEG) and transmission electron microscopy (TEM, JEOL 2010). Powder X-ray diffraction (XRD) patterns of the samples were recorded on a Philips X-Pert Pro X-ray diffractometer with Cu K_α radiation ($\lambda_{K\alpha1}$ = 1.5418 Å). X-ray photoelectron spectroscopy (XPS) analysis was performed on an ESCALAB 250 X-ray photoelectron spectrometer (Thermo, America) equipped with Al $K\alpha_{1,2}$ monochromatized radiation at 1486.6 eV X-ray source. The surface area and porosity of samples were measured by a Surface Area and Porosity Analyzer (Tristar 3020M). FT-IR spectra of the samples were obtained on a Perkin-Elmer TGA7 infrared spectrometer.

Electrochemical measurements.

Electrochemical measurements were conducted on an electrochemical work station (CHI 760D, CH Instruments, Inc., Shanghai, China) coupled with a PINE rotating disk electrode (RDE) system (Pine Instruments Co. Ltd. USA). A standard three-electrode electrochemical cell equipped with gas flow system was employed.

Prior to measurements, rotation disk electrode (RDE, 5.0 mm in diameter) was first polished with 5.0, 3.0 and 0.05 µm alumina slurry sequentially and then washed ultrasonically in water and ethanol for a few minutes, respectively. The cleaned electrode was dried with a high-purify nitrogen steam. Firstly, 20 µL of the prepared catalyst or commercial E-TEK Pt/C catalyst (2.0 mg mL^{-1}) was casted on the pretreated glassy carbon electrode and then dried at room temperature. In order to make the catalyst covered the entire glassy carbon electrode surface, another 20 µL of the catalyst was again casted on the pretreated glassy carbon electrode and dried at room temperature. A total catalyst volume of 40 µL was applied on glassy carbon electrode in this work. After that, 10 µL of Nafion (DuPont Corp., 0.05% in aqueous solution) was then placed on the surface of the above materials modified electrodes and dried at room temperature before electrochemical experiments.

The ORR performance of catalysts was studied by cyclic voltammogram (CV) and linear sweep voltammogram (LSV) measurements in an aqueous solution of 0.1 M KOH. CVs were measured at a scan rate of 50 mV s^{-1}. LSVs were measured at a scan rate of 10 mV s^{-1} under different disk rotation rates of 400, 625, 900, 1225 and 1600 rpm. All the potentials in this work were recorded with respect to the Ag/AgCl reference electrode. The obtained current values were normalized to the mass of the catalyst used (*i.e.*, given in mA mg^{-1}) for direct comparison between samples. For Koutecky-Levich analysis, the un-normalized currents obtained from measurements at varying rotation rates were used.

The number of electrons transferred per oxygen molecule was calculated by the Koutecky-Levich equation given below:[10]

$$J^{-1} = J_k^{-1} + \left(B\omega^{1/2}\right)^{-1} \quad (1)$$

$$B = 0.2nF\left(D_{O_2}\right)^{2/3}\nu^{-1/6}C_{O_2} \quad (2)$$

where J is the measured current density of the ORR, J_k is the kinetic current density, ω is the electrode rotating rate, B is the slope of K-L plots, n represents the number of electrons transferred per oxygen molecule, F is the Faraday constant ($F = 96485\ \mathrm{C}\cdot\mathrm{mol}^{-1}$), D_{O_2} is the diffusion coefficient of O_2 in 0.1 M KOH ($1.9\times10^{-5}\ \mathrm{cm}^2\cdot\mathrm{S}^{-1}$), ν is the kinetic viscosity ($0.01\ \mathrm{cm}^2\cdot\mathrm{S}^{-1}$), C_{O_2} is the bulk concentration of O_2 ($1.2\times10^{-3}\ \mathrm{mol}\cdot\mathrm{L}^{-1}$).[11] The constant 0.2 is adopted when the rotation speed is expressed in rpm.

Results and discussion

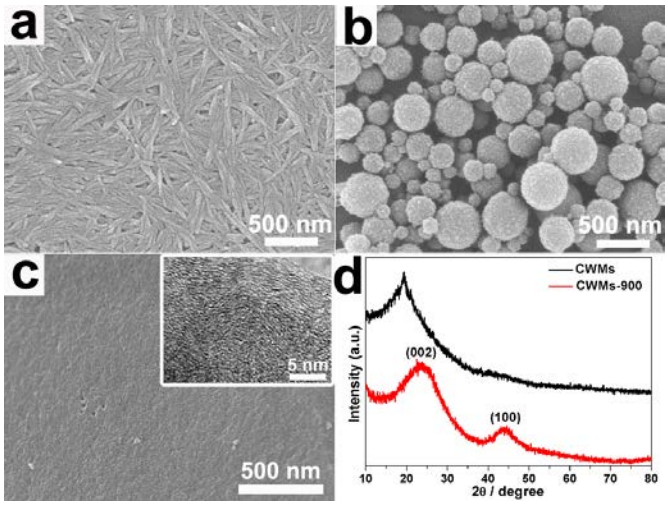

Fig. 1 (a) SEM image of CWs. (b) SEM image of CWMs. (c) SEM and HRTEM (inset) images of N-doped graphitic carbon product from direct pyrolysis of chitosan whisker microspheres at 900 °C (denoted as CWMs-900). (d) XRD patterns of CWMs and CWMs-900.

In this work, chitin was first extracted from low-cost and abundant crab shells by a series of chemical processes. Then uniformly

dispersed CWs were obtained by deacetylate treatment of chitin, exhibiting a length of ~500 nm and a diameter of ~50 nm (Fig. 1a). After a photochemical polymerization, the dispersed whiskers curled and assembled into spherical structures with diameters less than 500 nm and rough surface (Fig.1b). The FT-IR spectrum (Fig. S1, ESI†) of CWMs by photochemical polymerization reveals well-defined characteristic bands (1603, 1510, 1488, 1445 cm^{-1}) of styrene unit, and the peak at 1681 cm^{-1} is the characteristic band of carbonyl group (–C=O), suggesting that the compositions of CWMs contain the structural units of chitosan, PVP and DVB.[12] After a pyrolysis treatment at 900 °C, the microspheres assembled with chitosan whiskers transformed into compact graphitic carbon nanoparticles (CWMs-900) with sizes of ~10 nm and twisted graphitic layer structures, as shown in Fig. 1c and inset, which can be further confirmed by XRD characterization. In comparison with CWMs, the XRD pattern (Fig. 1d) of CWMs-900 shows two main peaks centered at 23° and 43°, corresponding to the (002) (2ϑ= 26.4°) and (100) (2ϑ= 42.8°) reflections of hexagonal graphite (JSPDS No. 00-001-0046). The shifted (002) reflection to a lower angle implies an increase in the interlayer spacing possibly owing to heteroatom (*e.g.*, N) doping into graphitic carbon structure.[13] This can be verified by the X-ray photoelectron spectra of CWMs-900. The XPS survey spectrum of CWMs-900 indicates the presence of C, N and O elements with N content of 2.51% (Fig. 2a). The N element is naturally originated from the components of crab shells, critically important for direct preparation of N-doped carbon nanostructure material for high efficient electrocatalytic applications.[14] The high resolution N1s spectrum (Fig. 2b) of CWMs-900 confirms two types of doped N in graphitic carbon structure, namely, pyridinic-N (398.3 eV) and graphitic-N (400.8 eV), both of them being suitable doping forms in carbon structure to contribute high ORR catalytic activity as demonstrated in literatures.[15]

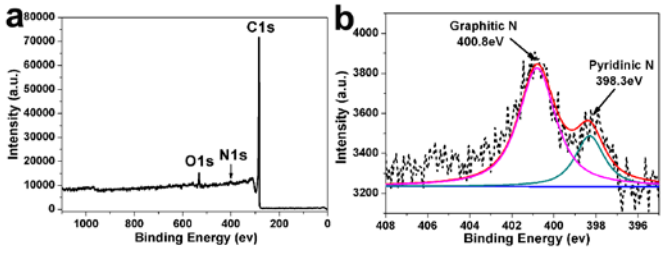

Fig. 2 (a) XPS survey spectrum, and (b) high resolution N1s spectrum of CWMs-900.

Further, the synthesized CWMs were used as precursors for adequately adsorbing $Fe(acac)_3$ under given experimental conditions. After that, no significant change in morphology was observed for CWMs (Fig. 3a). However, the spherical structures with $Fe(acac)_3$ transform into nonuniform particle-like structures after a pyrolysis treatment at 900 °C, as shown in Fig. 3b. Fig. 3c shows the XRD patterns of thermally transformed samples before and after HCl treatment. As shown, the pyrolyzed product before HCl treatment exhibits diffraction peaks attributed to graphitic carbon (JSPDS No. 00-001-0046), Fe_3C (JSPDS No. 00-006-0688), Fe_3O_4 (JSPDS No. 01-075-1609), Fe_2O_3 (JSPDS No. 01-089-8104) and Fe (JSPDS No. 01-087-0722), respectively, while only diffraction peaks of graphitic carbon and Fe_3C can be observed for the sample after HCl treatment. The above results deserve a further investigation. For the pyrolyzed sample before HCl treatment, TEM analysis demonstrates that the sample is composed of graphitic carbon skeleton and Fe-based components (*e.g.*, iron oxides, Fe_3C) (Fig. 3d, e). Importantly, it was found that the existence of iron oxides (*e.g.*, Fe_3O_4) in sample is completely independent and apart from graphitic carbon structure, while Fe_3C particles encapsulate into graphitic carbon structure to form a core-shell structure (Fig. 3d, e). This can be further confirmed by EDX spectra, in where O element is originated from independent iron oxide particles (Fig. 3f) and O element is completely disappeared for encapsulated Fe_3C particles in graphitic carbon structure (Fig. 3g). The HRTEM image (Fig. 3e) indicates that the independent spherical particle has a lattice space of 2.52 Å, corresponding to the (103) atom planes of Fe_3O_4, while the lattice space of core section in core-shell structure particle is 2.39 Å, corresponding to the (021) atom planes of Fe_3C, and the shell section in core-shell structure particle is well-ordered graphite layers with a lattice space of 3.39 Å, corresponding to the (002) atom planes of hexagonal graphite. After HCl treatment, other iron-based components can be completely removed from the thermally transformed sample (Fig. 3c), only Fe_3C nanocrystals encapsulated into graphitic carbon structure can be observed (Fig. 3c, h). Moreover, the encapsulated Fe_3C nanocrystals display high crystalline nature (Fig. 3i, j). The HRTEM image (Fig. 3i) of an individual core-shell structure further indicates that the lattice space of core section is 5.09 Å, corresponding to the (010) atom planes of Fe_3C, suggesting the formed Fe_3C nanocrystal cores with different exposed crystal facets in composite (Fig. 3e). This graphitic carbon-based core-shell structure with high crystalline Fe_3C nanocrystal core may be very beneficial for effectively improving catalytic activity and stability of composite for electrocatalysis applications.[2,6,7] The above results suggest that the chitosan whisker microspheres play important role in the formation of core-shell structure Fe_3C@NGC nanocomposite. During high temperature pyrolysis, the interior of chitosan whisker microspheres may be favourable for formation of a suitable growth atmosphere of Fe_3C nanocrystal cores, while the microsphere surface adsorbed $Fe(acac)_3$ may be more prone to forming independent iron oxide particles (*e.g.*, Fe_3O_4, Fe_2O_3) owing to the presence of microsphere surface rich O-containing function groups. To further verify this, the chitosan whiskers without photochemical polymerization after adsorbing $Fe(acac)_3$ were also thermally treated at 900 °C in N_2 in this work. The results demonstrate that the thermally transformed product is mainly composed of graphitic carbon and iron oxide particles (Fig. S2, ESI †), also indicating the importance of microsphere structure for forming graphitic carbon shell structure in Fe_3C@NGC composite.

Further, we also performed N_2 adsorption-desorption isotherm experiments of chitosan whisker microspheres after pyrolysis (CWMs-900) and Fe_3C@NGC samples. As shown in Fig. 4, a type IV of N_2 adsorption-desorption isotherm with a distinct hysteresis loop in high-pressure region (P/P_0>0.45-1.0) is obtained from CWMs-900 (black curve in Fig. 4a). The corresponding pore-size distribution curve (black curve in Fig. 4b) indicates the presence of micro- and

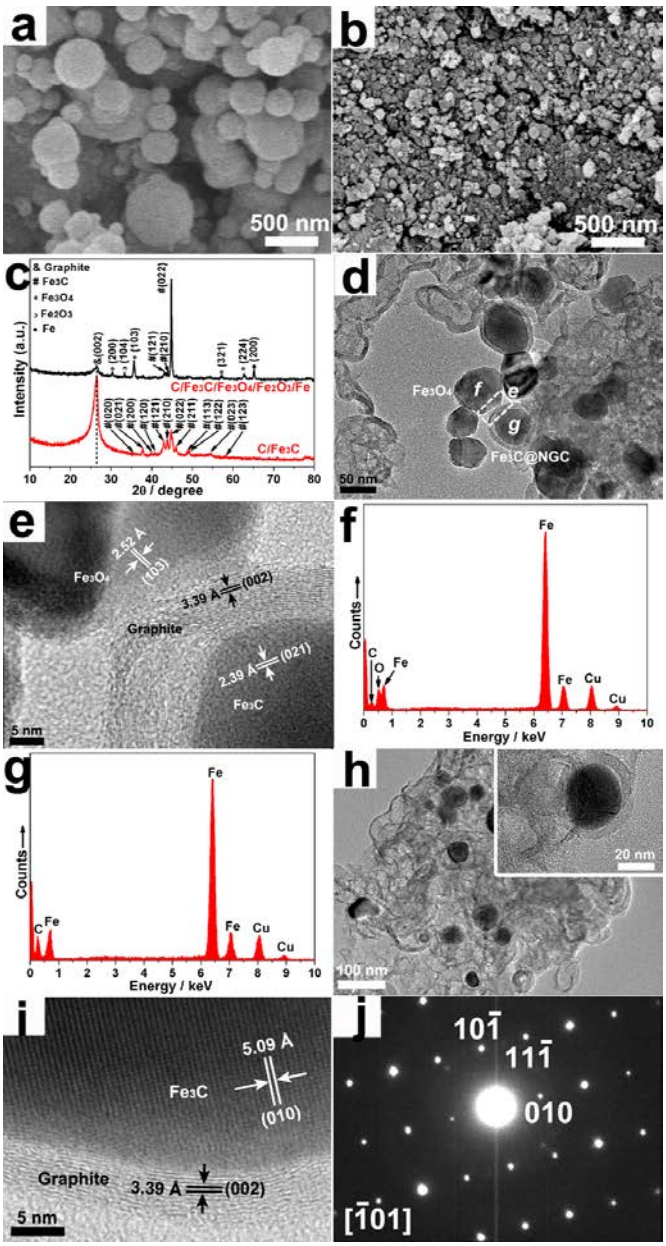

Fig. 3 (a) SEM image of CWMs after adsorbing $Fe(acac)_3$. (b) SEM image of thermally transformed sample. (c) XRD patterns of thermally transformed samples before and after HCl treatment. (d) TEM image, (e) HRTEM image, (f) and (g) EDX spectra at different locations of thermally transformed sample before HCl treatment. (h) TEM image, (i) HRTEM image and (j) corresponding SAED pattern of thermally transformed sample after HCl treatment.

meso-porous structures with a BET surface area of 608.5 $m^2 g^{-1}$, a pore volume of 0.34 $cm^3 g^{-1}$ and an average pore size of 2.2 nm. A similar N_2 adsorption-desorption isotherm was also obtained for Fe_3C@NGC sample (red curve in Fig. 4a). The BET surface area of Fe_3C@NGC was calculated to be 313.7 $m^2 g^{-1}$ with a pore volume of 0.31 $cm^3 g^{-1}$ and an average pore size of 4.0 nm. A detailed information is shown in Table S1 (ESI†). The large surface area of Fe_3C@NGC sample is very important as electrocatalyst for ORR application. More importantly, the porous structure of Fe_3C@NGC nanocomposite can effectively improve mass transfer of ORR-related species during electrocatalytic reaction, enabling full utilization of large catalytic active surface for high performance ORR.

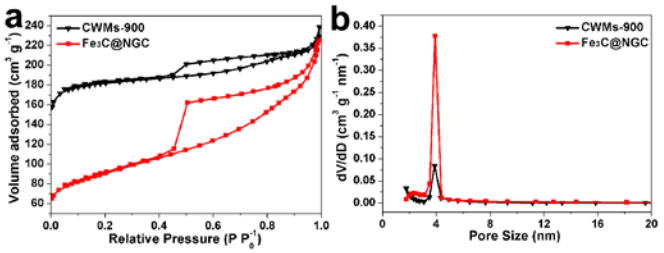

Fig. 4 (a) Nitrogen sorption isotherms and (b) pore size distributions of CWMs-900 and Fe_3C@NGC.

The ORR catalytic activity of Fe_3C@NGC sample as electrocatalyst was subsequently evaluated. For meaningful comparison, the measurements of CWMs-900 and commercial Pt/C coated glassy carbon (GC) electrodes were also performed under identical experimental conditions. Fig. 5a and 5b show the cyclic voltammetric (CV) curves of CWMs-900 and Fe_3C@NGC coated GC electrodes in N_2 or O_2 saturated 0.1 M KOH solutions. As shown, the cathodic current peaks at -0.37 V and -0.33 V can be apparently observed from the CV curves of CWMs-900 and Fe_3C@NGC coated GC electrodes, respectively. Anodic shift of *ca.* 40 mV for Fe_3C@NGC coated GC electrode indicates superior ORR activity compared to CWMs-900 coated GC electrode possibly attributing to a synergistic effect of Fe_3C nanocrystals and N doping in graphitic carbon creating more catalytic active sites. Fig. 5c shows the linear sweep voltammetric (LSV) curves of CWMs-900, Fe_3C@NGC and commercial Pt/C coated GC electrodes in O_2 saturated 0.1 M KOH solutions under a rotation rate of 1600 rpm with a sweep rate of 10 mV s^{-1}. As shown, the values of onset potential are -0.14 V, -0.09 V and -0.04 V for CWMs-900, Fe_3C@NGC and commercial Pt/C samples, respectively. Among all investigated catalysts, commercial Pt/C catalyst exhibits the lowest overpotential value, indicating the best ORR catalytic activity. In comparison with CWMs-900, Fe_3C@NGC catalyst indicates an intrinsic low overpotential value and relatively large cathodic current density for ORR application. As a key parameter, the transferred electron number in an ORR process determines a catalyst's efficiency.[16] Fig. 5d shows the Koutechy-Levich (K-L) curves of CWMs-900 coated GC electrode measured at different potentials (derived from LSV responses, inset in Fig. 5d). For a given potential, the measured current densities are directly proportional to the square root of the rotation rates for all cases investigated. Such linear relationships reveal a first-order reaction with respect to the dissolved O_2 concentration. From Fig. 5d, the transferred electron number (*n*) per O_2 molecule of CWMs-900 coated GC electrode was calculated to have an average value of 3.6 within the potential range of -0.5 V to -0.65 V, implying a four-electron ORR process.[17] The good ORR catalytic activity of CWMs-900 catalyst can be due to natural N doping with suitable doped types and level in graphitic carbon structure by pyrolyzing chitosan whisker microspheres.[18] In comparison with CWMs-900, Fe_3C@NGC catalyst indicates an average transferred electron number (*n*) of 3.8

within the potential range of -0.5 V to -0.65 V, more close to a four-electron ORR process (Fig. 5e).[19] The improved ORR catalytic activity can be ascribed to more catalytic active sites created by Fe_3C nanocrystals and N doping in graphitic carbon. The obtained results are comparable to the recent reported results using Fe_3C@carbon composite ORR catalysts.[2,6,7] The Tafel plots shown in Fig. 5f exhibit Tafel slopes of 180 mV dec^{-1}, 99 mV dec^{-1} and 69 mV dec^{-1} for CWMs-900, Fe_3C@NGC and Pt/C catalysts, respectively, indicating a relatively good kinetic process of Fe_3C@NGC sample for ORR. The resistant to crossover interference by fuel molecules is critically important for evaluating ORR catalysts. Fig. 5g shows the effect of 3.0 M methanol addition on the chronoamperometric responses of Fe_3C@NGC and Pt/C catalysts. It can be seen that Fe_3C@NGC coated GC electrode has an ability to tolerate the presence of 3.0 M methanol without noticeable crossover effects. This is critically important for practical ORR application of an electrocatalyst. The durability of Fe_3C@NGC coated GC electrode was also evaluated in an O_2-saturated 0.1 M KOH solution. As shown in Fig. 5h, only 10% decrease in the initial activity was observed from Fe_3C@NGC coated GC electrode, but a 24% decrease was observed from commercial Pt/C coated GC electrode under identical experimental conditions, confirming a high stability of Fe_3C@NGC coated GC electrode. This high catalytic stability may be attributed to the core-shell structured composite with very stable structure property in alkaline media.

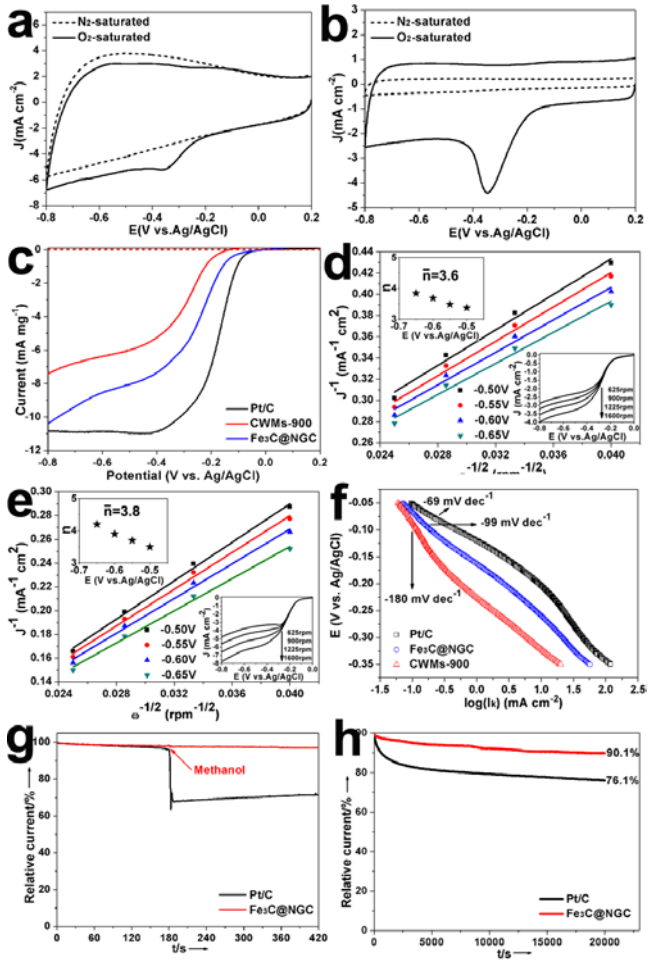

Fig. 5 (a) and (b) Cyclic voltammetry curves of CWMs-900 and Fe_3C@NGC electrocatalysts in N_2- and O_2-saturated 0.1 M KOH solutions at a scan rate of 50 mV s^{-1}. (c) LSVs of CWMs-900, Fe_3C@NGC and Pt/C electrodes in an O_2-saturated 0.1 M KOH solution (Scan rate = 10 mV s^{-1}, Rotation rate = 1600 rpm). (d) and (e) K-L plots (the bottom-right inset: corresponding LSVs, the top-left inset: calculated transferred electron numbers) of CWMs-900 and Fe_3C@NGC. (f) Tafel plots obtained from the RDE measurements of CWMs-900, Fe_3C@NGC and Pt/C at 1600 rpm. (g) Chronoamperometric responses of Fe_3C@NGC and Pt/C electrodes in O_2-saturated 0.1 M KOH (E_{app} = -0.35 V) with an addition of 1.0 ml of 3.0 M methanol at t = 180 s. (h) Durability of stability test for Fe_3C@NGC and Pt/C electrodes (E_{app} = -0.35 V, Scan rate = 10 mV s^{-1}, Rotation rate = 1600 rpm).

Although a real catalytic active mechanism is not very clear yet in this work, the ORR catalytic activity of Fe_3C@NGC can be proposed based on some related reports.[6,7,9,20,21,22] To sum up, the ORR catalytic activity of Fe_3C@NGC may be due to several aspects: (1) Suitable N doping types of graphitic-N and pyridinic-N result in the change of the surface charge and spin density in graphitic carbon, thus creating ORR catalytic active sites; (2) Shell layer of graphitic carbon can provide more graphene edge, thus introducing more catalytic active sites for ORR; (3) Core layer of Fe_3C nanocrystal with suitable exposed crystal facets is favourable for oxygen molecule adsorption, possessing superiorly electrochemical activity for ORR; (4) A synergistically electronic interaction between interior Fe_3C and outside graphitic carbon can effectively alter local electronic structure of the shell layer of graphitic carbon, thus resulting in the outer surface of graphitic carbon layer with high ORR activity. The above mentioned advantages of Fe_3C@NGC composite collectively contribute the high ORR catalytic performance.

Conclusions

In summary, Fe_3C nanocrystal@N-doped graphitic carbon (Fe_3C@NGC) nanocomposite was successfully fabricated using low-cost and earth-abundant crab shells as N-doped graphitic carbon source. It was found that the chitosan whisker microsphere structure obtained from crab shells is critically important for formation of core-shell structure Fe_3C@NGC nanocomposite. The resulting Fe_3C@NGC with large surface area as electrocatalyst shows good ORR catalytic activity in alkaline media possibly owing to a synergistic role of Fe_3C nanocrystals and N doping in graphitic carbon creating more catalytic active sites and a porous structure facilitating mass transfer to effectively improve the utilization of interior large catalytic active surface of catalyst. This work demonstrates the possibility of using low-cost and abundant biomass as material to fabricate high performance carbon-based electrocatalysts.

Acknowledgements

This work was financially supported by the Natural Science Foundation of China (Grant No. 51372248 and 51432009), the CAS/SAFEA International Partnership Program for Creative Research Teams of Chinese Academy of Sciences, China, and the CAS Pioneer Hundred Talents Program.

Notes and references

1 M. R. Gao, J. Jiang and S. H. Yu, *Small*, 2012, **8**, 13; H. Zhong, H. Zhang, G. Liu, Y. Liang, J. Hu and B. Yi, *Electrochem. Commun.*, 2006, **8**, 707; Y. Wang, S. Song, V. Maragou, P. K. Shen and P. Tsiakaras, *Appl. Catal., B: Environmental*, 2009, **89**, 223; K. Chen, X. Huang, C. Wan and H. Liu, *Chem. Commun.*, 2015, **51**, 7891.

2 Z. Y. Wu, X. X. Xu, B. C. Hu, H. W. Liang, Y. Lin, L. F. Chen and S. H. Yu, *Angew. Chem. Int. Ed.*, 2015.

3 L. Vočadlo, J. Brodholt, D. P. Dobson, K. S. Knight, W. G. Marshall, G. D. Price and I. G. Wood, *Earth. Planet. Sci. Lett.*, 2002, **203**, 567.

4 K. Tsutsumi, K. Nishimura and S. Sukawa, Kawasaki Heavy Ind Ltd (Kawj-C); Y.-z. Chan, Y. Dai, R. Li, J.-l. Zou, G.-h. Tian and H.-g. Fu, *Carbon*, 2015, **89**, 8; G. Li, L. Wang, W. Li and Y. Xu, *Microporous Mesoporous Mater.*, 2015, **211**, 97.

5 R. Zhang and W. Chen, *Sci. Bull.*, 2015, **60**, 522.

6 G. Zhong, H. Wang, H. Yu and F. Peng, *J. Power Sources*, 2015, **286**, 495.

7 W. Yang, X. Liu, X. Yue, J. Jia and S. Guo, *J. Am. Chem. Soc.*, 2015, **137**, 1436.

8 K. Ai, Y. Liu, C. Ruan, L. Lu and G. M. Lu, *Adv. Mater.*, 2013, **25**, 998.

9 Y. Li, H. Zhang, Y. Wang, P. Liu, H. Yang, X. Yao, D. Wang, Z. Tang and H. Zhao, *Energy Environ. Sci.*, 2014.

10 A.J. Bard, L. Faulkner, *Electrochemical Methods*, Wiley, NewYork, 1980.

11 R. Davis, G. Horvath and C. Tobias, *Electrochim. Acta*, 1967, **12**, 287.

12 A. Sionkowska, M. Wisniewski, J. Skopinska, S. Vicini and E. Marsano, *Polym. Degrad. Stab.*, 2005, **88**, 261.

13 Y. Wu, S. Fang, Y. Jiang and R. Holze, *J. Power Sources*, 2002, **108**, 245.

14 Y. Li, H. Zhang, P. Liu, Y. Wang, H. Yang, Y. Li and H. Zhao, *Electrochem. Commun.*, 2015, **51**, 6.

15 Z.-H. Sheng, L. Shao, J.-J. Chen, W.-J. Bao, F.-B. Wang and X.-H. Xia, *Acs Nano*, 2011, **5**, 4350; J. Xu, Y. Zhao, C. Shen and L. Guan, *ACS Appl. Mater. Interfaces*, 2013, **5**, 12594; L. Lai, J. R. Potts, D. Zhan, L. Wang, C. K. Poh, C. Tang, H. Gong, Z. Shen, J. Lin and R. S. Ruoff, *Energy Environ. Sci.*, 2012, **5**, 7936.

16 K. Gong, F. Du, Z. Xia, M. Durstock and L. Dai, *Science*, 2009, **323**, 760; L. Dai, Y. Xue, L. Qu, H. J. Choi and J. B. Baek, *Chem. Rev.*, 2015, **115**, 4823; Z. L. Wang, D. Xu, J. J. Xu and X. B. Zhang, *Chem. Soc. Rev.*, 2014, **43**, 7746; B. C. H. Steele and A. Heinzel, *Nature*, 2001, **414**, 345.

17 H. Zhang, Y. Wang, D. Wang, Y. Li, X. Liu, P. Liu, H. Yang, T. An, Z. Tang and H. Zhao, *Small*, 2014, **10**, 3371.

18 T. X. Wu, G. Z. Wang, X. Zhang, C. Chen, Y. X. Zhang and H. J. Zhao, *Chem. Commun.*, 2015, **51**, 1334.

19 J. Liang, Y. Jiao, M. Jaroniec and S. Z. Qiao, *Angew. Chem. Int. Ed.*, 2012, **51**, 11496.

20 W. Yang, Y. Zhai, X. Yue, Y. Wang and J. Jia, *Chem. Commun.*, 2014, **50**, 11151.

21 X. Zheng, J. Deng, N. Wang, D. Deng, W. H. Zhang, X. Bao, C. Li, *Angew. Chem., Int. Ed.*, 2014, **53**, 7023.

22 H. T. Chung, J. H. Won, P. Zelenay, *Nat. Commun.*, 2013, **4**, 1922.